

**Influence of crystal orientation on pattern formation of focused-ion-beam milled Cu surfaces**Maria Lenius,<sup>1</sup> Reiner Kree,<sup>2,\*</sup> and Cynthia A. Volkert<sup>1</sup><sup>1</sup>*Institut für Materialphysik, Universität Göttingen, D-37077 Göttingen, Germany*<sup>2</sup>*Institut für Theoretische Physik, Universität Göttingen, D-37077 Göttingen, Germany*

(Received 16 February 2011; published 29 July 2011)

The erosion profiles of Cu surfaces after focused ion beam sputtering have been investigated as a function of crystal orientation and ion beam incidence. We find that all patterns are aligned with crystallographic axes and have wavelengths of about  $0.5 \mu\text{m}$ . The patterns depend strongly on the crystal orientation, typically with similar patterns for neighboring orientations, but may also be influenced by the ion beam direction. For orientations close to  $\{100\}$ , we find however that surfaces stay smooth for all incidence angles. The results are discussed in the context of current continuum models and indicate that modifications to the models are required to account for the effect of crystal orientation.

DOI: [10.1103/PhysRevB.84.035451](https://doi.org/10.1103/PhysRevB.84.035451)

PACS number(s): 68.35.-p, 61.80.Jh

**I. INTRODUCTION**

The development of complex patterns at ion-sputtered surfaces of metals and semiconductors has been intensely investigated over the past decades. The study of surface evolution during sputtering enables new insights into non-equilibrium processes<sup>1</sup> and has a number of potential applications for the selective preparation of nanoscale structures (e.g., for optics).<sup>2</sup>

The first systematic theory of surface pattern formation during ion beam erosion on amorphous substrates was the continuum approach of Bradley and Harper (BH),<sup>3</sup> based on previous work of Sigmund.<sup>4</sup> They attributed patterning to the interplay of thermal diffusion and a curvature-dependent sputter yield. Diffusion tends to smoothen, whereas the latter effect roughens the surface. More recently, this theory has been extended in a number of ways. In particular, a further smoothing mechanism has been added that corresponds to a downhill current density on the surface,<sup>5,6</sup> possibly because of momentum transfer from the impinging ion. The concerted action of these mechanisms can either result in stable smooth surfaces or lead to the formation of surface structures.

Semiconductors, which are easily amorphized at the surface during ion beam erosion, should be an ideal model system for the continuum theory. A number of previous experimental studies had shown a wide spectrum of interesting nanoscale patterns, including ripples, but also ordered arrays of dots.<sup>7,8</sup> More recently, it has been observed that metal impurities at the surface have a pronounced influence on pattern formation and that in their absence, flat surfaces are remarkably stable over a wide range of ion incidence angles.<sup>9–11</sup> Lately, Madi *et al.* have shown that impact-induced atomic redistribution may be a decisive factor for the transition from flat surfaces at low angles to rippled surfaces at high incidence angles.<sup>12</sup> Experiments also show that the characteristic wavelength near a pattern-changing instability does not always diverge, as is predicted by the continuum theory. Thus, recent experiments imply that pattern formation by ion beam erosion is less well understood than was previously thought.

For metal substrates, the situation is complicated by the stable crystal structure, so that the validity of the isotropic continuum theory is challenged from the outset. Furthermore, pattern formation is likely influenced by the presence of anisotropic surface diffusion and non-equilibrium uphill

currents, which can emerge from modified energetic barriers at step edges, known as Ehrlich–Schwoebel (ES) barriers and from fast edge diffusion.<sup>1,13,14</sup> The modified barriers have the same order of magnitude as the activation energies for surface diffusion and depend on the crystal orientation (see Table I for some values for low-index Cu surfaces). Fast edge diffusion has been included in kinetic Monte Carlo simulations of adatom motion,<sup>15,16</sup> but not yet in continuum models.<sup>1</sup> It leads to more compact shapes, which enhances the island nucleation rate on terraces. The non-equilibrium currents of adatoms may induce self-organized mound-and-pit or cone patterns,<sup>17</sup> as is typically observed in crystal growth and molecular beam epitaxy.<sup>14,19</sup> Thus, the patterns of ion-irradiated metal surfaces result from a complex interplay of ion-impact-induced effects and thermally driven surface currents. One way to partly disentangle these effects is to study pattern morphologies at different sputtering conditions such as temperature, incidence angle, ion energy, or ion flux. In particular, both at high and low temperatures, uphill non-equilibrium currents are less important, and the pattern formation is dominated by BH-type ripples oriented relative to the ion beam direction. At intermediate temperatures, one may enter a regime wherein the thermally driven currents generate patterns, which grow faster than the BH ripples and are oriented relative to the surface crystal anisotropy. The transition between these two regimes, which are also referred to as erosive and diffusive regimes, respectively, has been studied in detail on Cu (001) surfaces.<sup>1</sup>

To describe these effects, a continuum model has been put forward that combines erosion terms as derived for amorphous substrates with the above-mentioned anisotropic diffusion and ES currents taken into account in a gradient expansion.<sup>18</sup> Because the continuum description is based on the assumption of a small slope, it may be limited to the initial stages of pattern formation. This model was used successfully to explain data of an ion beam erosion study at a Cu(110) surface by Rusponi *et al.*<sup>20</sup> The main findings of this study are, first, that ripples emerge for normal ion incidence along crystallographic directions that depend on the surface temperature. Second, off-normal sputtering produces ripples whose in-plane orientation depends on the ion beam incidence angle  $\Theta$ , as well as on the azimuthal angle  $\Phi$ .

TABLE I. Activation energy and ES barriers for low-index Cu surfaces.

	$E_D$ (eV) <sup>a</sup>	$E_s$ (eV) <sup>a</sup>
Cu(100)	0.43	0.14
Cu(110) $\langle 1\bar{1}0 \rangle$	0.29	0.19
Cu(110) $\langle 001 \rangle$	0.42	0.27
Cu(111)	0.05	0.31

<sup>a</sup>Reference 27.

The present work addresses the question of whether the findings, obtained on a few low-index surface orientations, are generic for all crystal orientations. We have investigated ion beam-induced pattern formation on a large variety of Cu surface orientations. Although all our patterns are oriented with respect to crystal anisotropies, we find that pattern formation is usually more complex than on Cu(110), for which our results agree with those of Rusponi *et al.*<sup>20</sup> The patterns depend strongly on surface orientation but may also be influenced by the ion beam direction. Because of a lack of diffusivity data for the surface orientations studied here, we cannot aim at a quantitative comparison of our results with the continuum theory put forward in Ref. 18. Nevertheless, we will argue that additional orientation-dependent physical mechanisms, which have not yet been identified, have to be added to the proposed continuum theory to reach consistency with our findings.

## II. EXPERIMENTAL TECHNIQUES

Most experiments were performed on a centimeter-sized piece of 99.99% pure and 100- $\mu\text{m}$ -thick as-rolled Cu foil, which was annealed at  $1 \times 10^{-6}$  mbar for 24 h at a temperature of 700 °C to obtain large grains by recrystallization. The resulting grain orientations were measured by electron backscattering diffraction (EBSD). The sample was then electropolished with a 3:7 mixture of 85% phosphoric acid and deionized water at 1.5 V to remove surface damage. The remaining surface roughness due to etching was between 5.5 and 9.5 nm, depending on the crystal orientation. A few additional experiments were performed on a (123)-oriented single crystal grown by the Bridgman technique, which allowed large ion beam parameter variation studies on a single crystal orientation. To minimize surface oxidation, the Cu samples were stored in a desiccator. Any residual oxide layer was removed during the beginning of the sputtering process.

Sputter erosion studies presented here were carried out in a FEI Nova NanoLab 600 Focused Ion Beam (FIB) microscope with a base pressure of  $\leq 5 \times 10^{-5}$  mbar and equipped with an integrated scanning electron microscope (SEM). All studies were performed at room temperature. Square regions (10  $\mu\text{m}$  by 10  $\mu\text{m}$ ) inside single grains were exposed to a 30-keV Ga<sup>+</sup> ion beam with a full width at a half-maximum diameter of 81 nm and doses between 0.83 and  $10.31 \times 10^{17}$  ions/cm<sup>2</sup>. During the milling process, the ion beam was scanned in a serpentine raster using 40.5-nm-spaced raster points, each with a dwell time of 1  $\mu\text{s}$ . Compared with other sputter techniques, high ion fluxes of  $3.7 \times 10^{20}$  ions/(cm<sup>2</sup>s) are thereby achieved

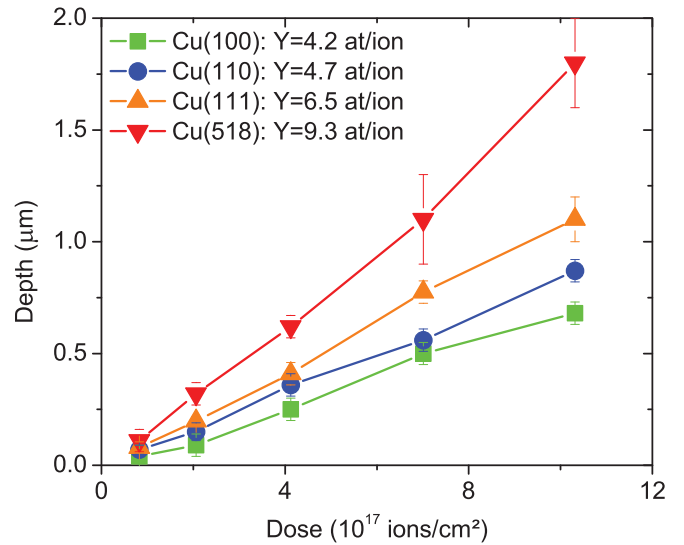


FIG. 1. (Color online) The dependence of the sputtered depth on the ion dose for Cu(100) (flat surface), Cu(110) (ripples), Cu(111) (craters), and Cu(518) (sawtooth structure). The sputter yield  $Y$  is determined from the slopes.

at each raster point. Erosions were performed under normal ion incidence, as well as at 15°, 30°, 45°, and 62°.

The surface topography after milling was analyzed using the SEM of the FIB system, as well as an atomic force microscope (AFM; Asylum MFP-3D). The AFM results presented here were recorded in the intermittent contact mode with a scan speed of 10  $\mu\text{m}/\text{s}$  and have a resolution of 256 pixels  $\times$  256 pixels. The nominal tip radius was about 6 nm. Length scales and periodicities of the self-organized structures were analyzed with the help of power spectra. The sputtered depth was also measured by AFM, although the steep edges of the sputtered regions produced errors, particularly for the largest depths.

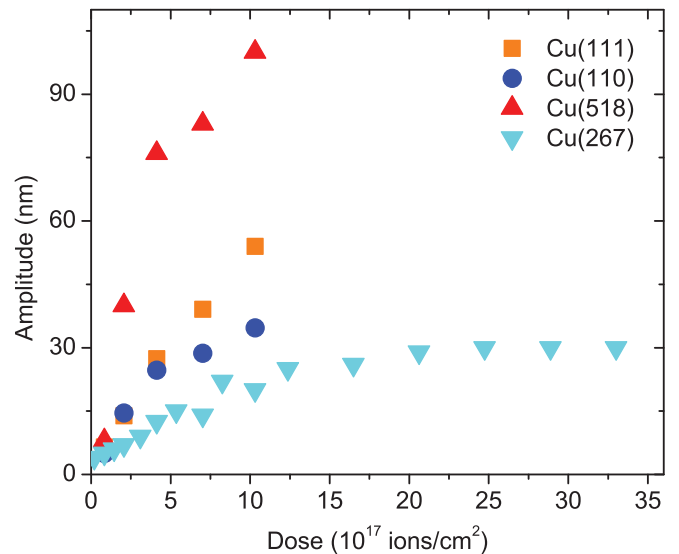


FIG. 2. (Color online) Evolution of the pattern amplitudes with increasing dose for Cu(111) (craters), Cu(110) (ripples), Cu(518) (sawtooth structure), and Cu(267) (ripples).

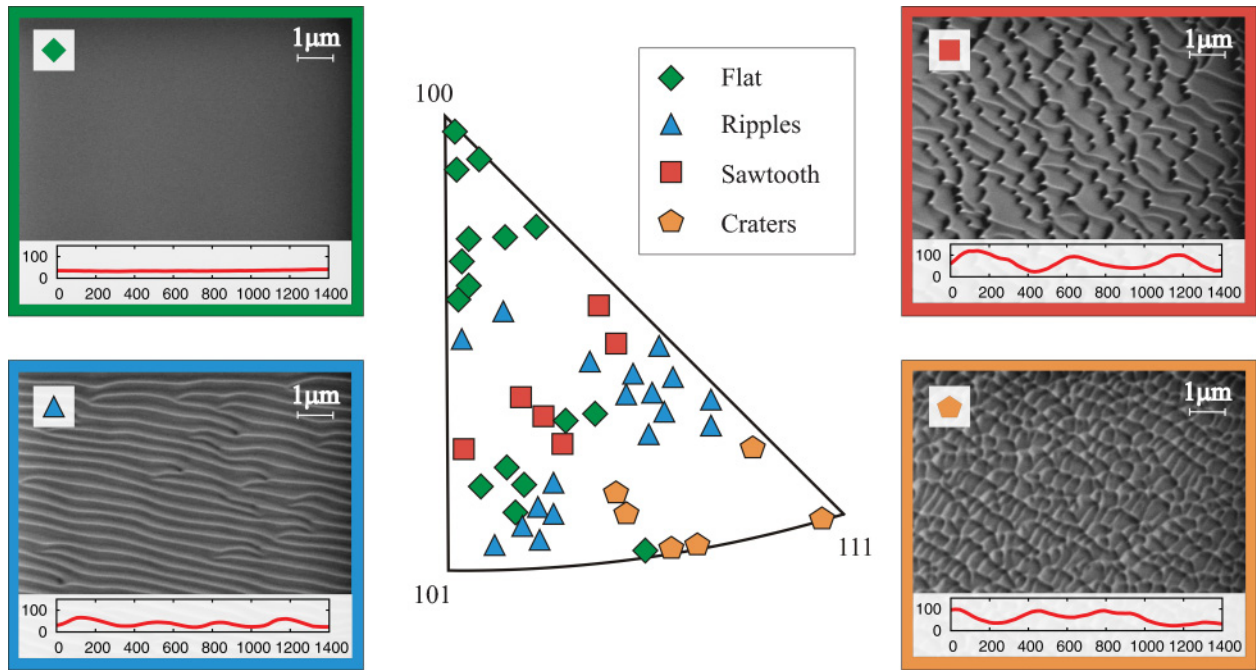


FIG. 3. (Color online) SEM images of the different topographies on Cu after Ga ion beam erosion with 30 keV and doses of  $7.01 \times 10^{17}$  ions/cm<sup>2</sup>. The insets show the height profiles in units of nm obtained from AFM scans perpendicular to the main pattern features. The crystal orientations for which these patterns occur at normal ion beam incidence are marked in the inverse pole figure.

For estimating the gallium influence on the pattern formation, the Ga distribution in two grains was determined in a scanning transmission electron microscope (STEM; Philips CM12) with an integrated energy dispersive x-ray (EDX) spectrometer based on a Ge detector. The STEM images have been made with a voltage of 120 kV and a spot size of 10 nm using a semiconductor near axes detector. The two investigated grains had orientations of Cu(100) and Cu(518) and were eroded with doses of  $4.12 \times 10^{17}$  ions/cm<sup>2</sup> and  $7.01 \times 10^{17}$  ions/cm<sup>2</sup> under normal ion incidence, respectively. Two cross-sectional TEM-foils were then cut in the eroded surfaces with a standard FIB preparation technique, as described in Ref. 21. A Pt-based film was deposited on the Cu surface before fabrication of the TEM lamella to protect the surface from further ion beam damage and to minimize Ga implantation. Finally, the TEM lamella was transferred to a molybdenum TEM grid by micromanipulation.

III. RESULTS

All patterns for all orientations have in common that they are not aligned with the ion beam but with crystallographic axes. However, the orientation of the developing structures can be partly influenced by the direction of ion beam incidence; for instance, alignment with different crystallographic axes can be instigated by tilting the ion beam. The sputtering process is characterized by an orientation-dependent linear increase of the milling depth with dose, as shown in Fig. 1. Although the data extrapolates through the origin, the scatter in the data cannot rule out different sputter yields for pure and Ga-doped Cu. However, the constant sputter yield shows no influence of the evolving structures. The amplitude of developing structures increases with a power law dependence on dose and reaches a height of 20–100 nm after an ion dose of  $10^{18}$  ions/cm<sup>2</sup> (see

Fig. 2). Prolonged sputtering at greater than  $10^{18}$  ions/cm<sup>2</sup> can lead to a saturation of the amplitude, as demonstrated for the ripple structure on the Cu(267) surface. The wavelengths of the surface morphologies are between 200 and 500 nm, depending on the grain orientation and the type of pattern. Studies as a function of beam current and beam focus performed on the single crystal indicate furthermore that the patterns are not rate dependent for ion fluxes between  $7.4 \times 10^{15}$  and  $3.7 \times 10^{20}$  ions/(cm<sup>2</sup>s), as well as not dependent on the

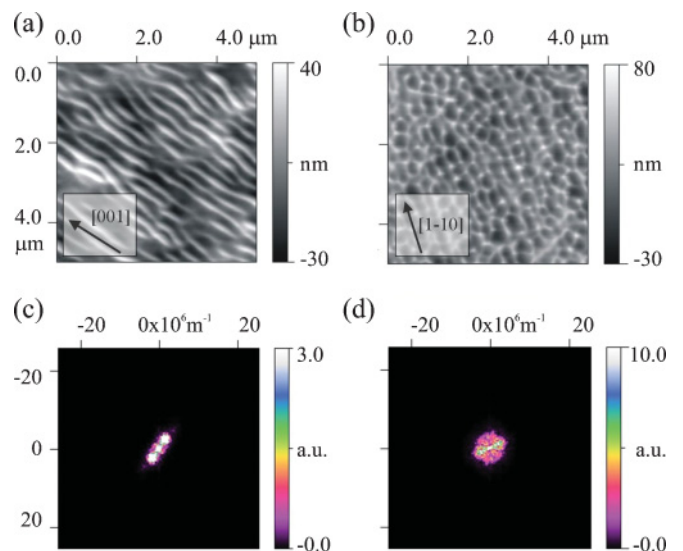


FIG. 4. (Color online) AFM images of (a) Cu(110) and (b) Cu(111) after 30 keV Ga<sup>+</sup> erosion under normal ion incidence with doses of  $7.01 \times 10^{17}$  ions/cm<sup>2</sup> and the corresponding power spectra (c, d), which reveal the symmetries and periodicities of the patterns.

TABLE II. Experimentally observed patterns<sup>a</sup> after sputtering Cu surfaces of different orientations. In addition to normal sputtering, the surfaces were rotated around an in-plane axis to vary the ion incidence angle  $\Theta$  from  $0^\circ$  to  $62^\circ$ . For Cu(1 0 0), 16 in-plane rotation axes spaced at  $22.5^\circ$  were used. The orientation of ripples is additionally indicated by their angle relative to the direction perpendicular to the ion beam projection.

Surface orientation	Rotation axis	$\Theta = 0^\circ$	$\Theta = 15^\circ$	$\Theta = 30^\circ$	$\Theta = 45^\circ$	$\Theta = 62^\circ$
Cu(1 0 0)	e.g.(15 25 $\bar{2}$ )	f	f	f	f	f
Cu(1 0 1)	(11 19 $\bar{12}$ )	r(62°)		r(52°)	r(55°)	r(59°)
Cu(1 1 1)	(14 $\bar{19}$ 7)	c	c	c	c	r(108°)
Cu(3 16 19)	(20 $\bar{13}$ 7)	r(40°)	r(51°)	r(32°)	r(40°)	r(57°)
Cu(7 2 24)	(0 25 $\bar{2}$ )	f	f	f	f	f
Cu(2 2 25)	(0 25 $\bar{2}$ )	f	f	f	f	f
Cu(1 5 24)	(25 $\bar{2}$ 0)	f	r(100°)	f	f	f
Cu(0 7 24)	( $\bar{21}$ 13 $\bar{4}$ )	f	f	f	f	f
Cu(9 7 22)	(13 18 $\bar{11}$ )	s	s	r(88°)	f	f
Cu(5 5 7)	( $\bar{9}$ $\bar{16}$ 17)	c	c	f	f	r(61°)
Cu(4 16 19)	( $\bar{19}$ $\bar{11}$ 12)	r(134°)		r(148°)	r(143°)	r(105°)
Cu(2 6 7)	( $\bar{21}$ $\bar{7}$ 12)	r(132°)	f	r(150°)	r(142°)	r(147°)
Cu(1 1 6)	(25 $\bar{2}$ $\bar{4}$ )	f	f	f	f	f
Cu(10 8 21)	( $\bar{2}$ $\bar{11}$ 5)	r(43°)	r(43°)	r(41°)	r(42°)	r(49°)
Cu(7 13 20)	( $\bar{18}$ $\bar{11}$ 13)	r(116°)	r(113°)	f	f	f
Cu(13 8 20)	(17 10 $\bar{15}$ )	r(112°)	f	f	s	r(118°)
Cu(13 4 21)	(6 23 $\bar{8}$ )	s	r(57°)	r(40°)	f	f
Cu(11 9 21)	( $\bar{9}$ $\bar{19}$ 13)	r(70°)	c	r(51°)	r(56°)	r(62°)
Cu(6 12 21)	( $\bar{19}$ $\bar{12}$ 12)	c	r(117°)	f	f	f
Cu(8 4 9)	(5 8 $\bar{8}$ )	c	r(67°)		s	s
Cu(5 13 21)	(23 6 $\bar{8}$ )	f	r(130°)	r(135°)	r(131°)	r(130°)
Cu(2 0 3)	(13 20 $\bar{9}$ )	r(57°)	r(65°)	r(57°)	r(51°)	f
Cu(10 1 23)	(1 $\bar{25}$ 0)	r(0°)	r(0°)	r(90°)	r(0°)	f
Cu(5 6 10)	( $\bar{21}$ $\bar{5}$ 13)	r(107°)	c	r(98°)	r(73°)	f
Cu(16 7 18)	(17 $\bar{16}$ $\bar{9}$ )	c	f	c	s	r(103°)
Cu(3 17 18)	( $\bar{15}$ 16 $\bar{12}$ )	r(62°)	r(61°)	r(61°)	r(62°)	f
Cu(17 7 17)	( $\bar{10}$ $\bar{16}$ 17)	f	r(55°)	r(55°)	r(60°)	r(62°)
Cu(3 16 19)	( $\bar{18}$ $\bar{12}$ 13)	r(108°)		r(116°)	r(117°)	f
Cu(8 16 17)	( $\bar{18}$ $\bar{7}$ 16)	c	r(124°)	c	c	s
Cu(2 9 23)	(25 2 $\bar{3}$ )	r(157°)	r(158°)	r(158°)	r(143°)	r(152°)
Cu(15 1 20)	(15 $\bar{17}$ $\bar{10}$ )	f	r(126°)	r(123°)	r(118°)	r(111°)
Cu(15 4 19)	(1 1 $\bar{1}$ )	r(78°)	f	r(76°)	r(72°)	r(73°)
Cu(5 1 8)	(12 20 $\bar{9}$ )	s	r(67°)	r(70°)	f	f
Cu(16 2 19)	(8 $\bar{24}$ $\bar{3}$ )	f	r(133°)	r(134°)	r(146°)	s
Cu(8 6 23)	(11 4 $\bar{5}$ )	s	s	s	f	f

<sup>a</sup>Abbreviation: f, flat; r, ripples; s, sawtooth profile; c, craters.

ion beam diameter for diameters between 19 and 405 nm. This behavior can be attributed to the fact that even for the highest fluxes the average time between two cascades,  $10^{-11}$  s, is comparable or smaller than the average duration of one cascade.<sup>22</sup>

Despite the differences in wavelength, amplitude, and regularity, the patterns can be classified into four groups. As displayed in Fig. 3, sputtered surfaces can stay flat or even smoothen or develop ripples, craters, or a pronounced sawtooth profile. Characteristic profiles are shown in the inset of each image for each pattern type. Note that most features have small slopes; however, some change on length scales, coming close to the size of a collision cascade. For normal ion incidence, the occurrence of patterns from the four pattern groups is correlated with surface crystal orientation, and shows a tendency to cluster, as illustrated in the inverse

pole figure (IPF) in Fig. 3. Flat surfaces are rather found for grains with crystal orientations close to  $\{100\}$ , whereas craters mainly developed around  $\{111\}$ . Ripples and sawtooth-profiled structures evolve in the middle of the IPF.

The orientation of the patterns differs for the diverse grains. As shown in Fig. 4, the surface structures on the low-index surfaces of (a) Cu(110) and (b) Cu(111) are aligned with the low-index crystallographic axes of (a)  $[001]$  and (b)  $[\bar{1}10]$ ,  $[1\bar{1}0]$ , and  $[0\bar{1}1]$ , respectively. The threefold symmetry of the Cu(111) surface pattern is more obvious in the power spectrum (d). The slight preference for the  $[1\bar{1}0]$  direction, as seen in Figs. 4(b) and 4(d), is probably due to a slight deviation away from (111) by  $2.5^\circ$ . In contrast, on high-index surfaces, the patterns are not aligned with low-index crystallographic axes, but rather with the direction that corresponds to the intersection of the surface with  $\{100\}$  or  $\{111\}$  planes.

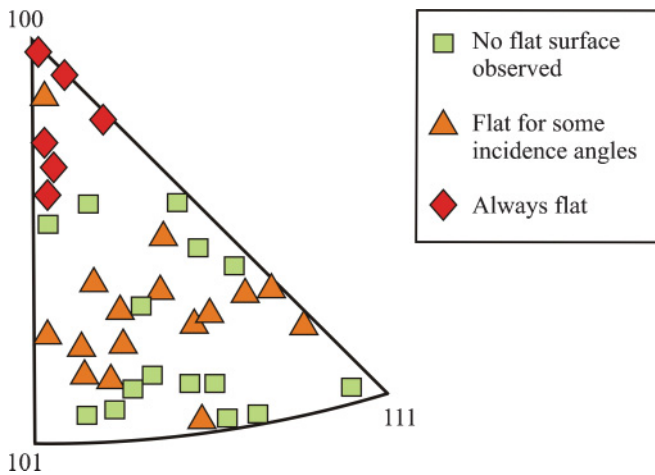


FIG. 5. (Color online) Surfaces with different crystallographic orientations were eroded under 0°, 15°, 30°, 45°, and 62° ion beam incidence. The IPF displays for which orientations flat surfaces are found.

Ion beam tilting can result in different surface topographies. For instance, by rotating the ion beam around the (9 16 17) in-plane axes, Cu(557) develops craters under 0° and 15° ion incidence, remains flat under 30° and 45°, and forms ripples under 62°. Further scenarios of more surface orientations are summarized in Table II. In general, changes between all pattern groups (flat, ripples, craters, and sawtooth profile) are observed. For most surface orientations no, one, or two transitions occur, but also three and four transitions, as for Cu(16 7 18) are found. Conspicuously frequent are transitions from craters and sawtooth profiles to ripples. Figure 5 depicts additionally for which crystal orientation flat surfaces are found. It shows that the surfaces around the {100} orientation stay smooth for all incidence angles. On grains with orientations close to {110} or {111}, no flat surfaces, but ripples and craters, develop for all incidence angles, which sometimes change their in-plane alignment with ion beam incidence (see also Table II). Note that this rotation is not necessarily toward the ion beam direction, as is often observed for amorphous materials. Most grains in the middle of the IPF show complicated behavior,

including changes between smooth surfaces and different patterns as a function of incidence angle.

The Ga distribution of Cu(100) with a smooth surface and of Cu(518) with a sawtooth-profile surface was measured with EDX to estimate the influence of the Ga impurities on the pattern formation. It was found that the Ga concentration increases in the first 15 nm to approximately 20 and 8 at% on Cu(100) and Cu(518), respectively, and that it decreases to the background level again within the next 15 nm (Fig. 6). Cu-Ga intermetallic phases can be formed when the Ga concentration exceeds 20 at%.<sup>23</sup> However, no gallium precipitation was found either by imaging or selected-area diffraction, and no significant difference in Ga concentration was measured between the crests (Fig. 6(b)) and troughs (Fig. 6(c)) of the pattern.

IV. DISCUSSION

All patterns in this work are aligned with crystallographic axes, which indicates sputtering in the diffusive regime.<sup>18</sup> The results show that the crystal orientation of the surface plays a decisive role for pattern formation at both normal and oblique ion incidence. The patterns are very complex, especially with respect to changes in incidence angles. A discussion of Rusponi’s and Valbusa’s theory<sup>18,20</sup> shall now be applied to see whether our results can be explained by this model. This theory was developed primarily to explain results of an erosion study on Cu(110) performed by Rusponi *et al.*

First note that our results for Cu(110) do not contradict what Rusponi found. They observed ripples aligned with [001] for normal Ar incidence at 250 K, and for 45° at 180 K. Under 70° at 180 K, the ripples were aligned with the ion beam. We performed measurements under 0°, 45°, and 62° at room temperature, and we obtained ripples that were aligned with [001] for all angles.

The theoretical description<sup>18,20</sup> combines erosion terms, ES surface diffusion terms, and downhill diffusion or Carter–Vishnyakov (CV) smoothing terms in a gradient expansion and is thus only applicable for small slopes. This model is considered here for the general crystal orientations experimentally explored in this study. To test the local stability

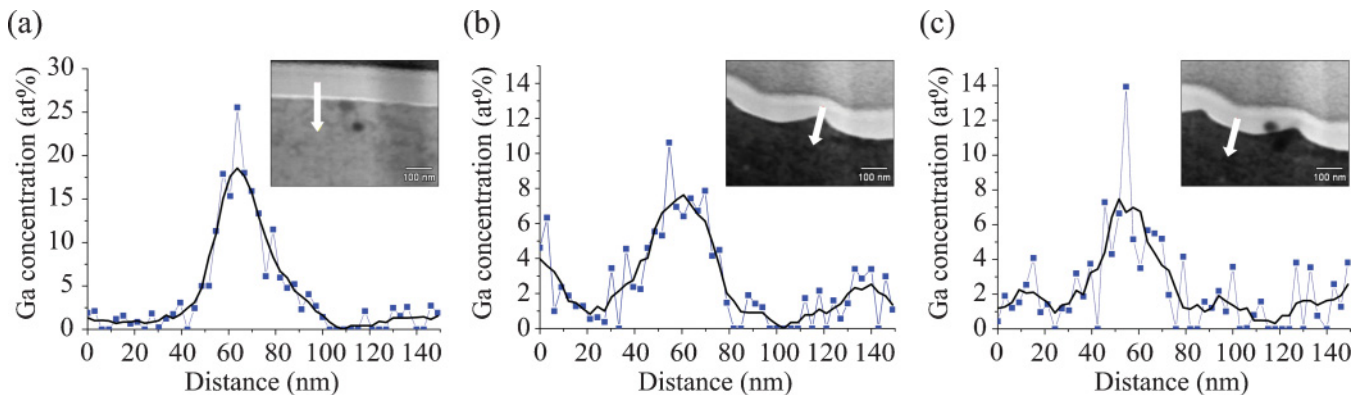


FIG. 6. (Color online) Measured EDX profile (dots) in STEM and five-point adjacent average (solid line) of eroded (a) Cu(100) and (b,c) Cu(518). The profile in panel b was measured through a crest, and in panel c through a trough of the ripple pattern on Cu(518). The STEM images in the insets show where the line scans were acquired (indicated by the white arrow). The darker, lower part of the picture corresponds to Cu, whereas the lighter part shows the protective platinum film.

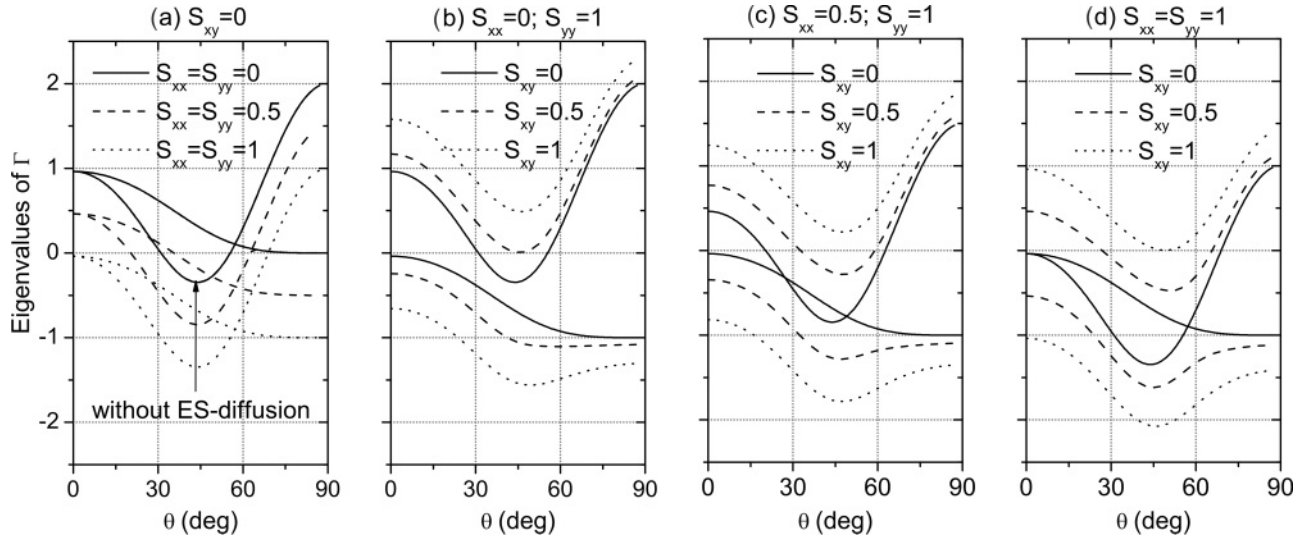


FIG. 7. The two eigenvalues of  $\Gamma$ , which represent the growth rates of small-amplitude fluctuations, are plotted as a function of the ion incidence angle  $\Theta$  for varying ES barriers. Negative values indicate instabilities of a flat surface. The CV smoothing term is chosen large enough to ensure a stable flat surface in the absence of ES barriers, except in a region of  $\Theta$  around  $40^\circ$ , where negative values are always predicted. The solid line (a) depicts a typical plot without ES barriers. The curves for finite ES barriers are calculated using appropriate nonvanishing values of the  $S$  coefficients. Generally, this leads to splitting and shifting of the eigenvalue curves. Despite these changes, an unstable region and a maximum at  $\Theta = 0^\circ$  always occur. Scenarios in which an unstable flat surface at small  $\Theta$  changes into a stable flat surface with increasing  $\Theta$  never occur.

of a flat surface, only terms up to linear order in the surface height profile  $h(x, y, t)$  need to be taken into account. Within this model, the erosion term and the CV term depend on the ion incidence angle  $\Theta$ , but not on the azimuthal orientation  $\Phi$  on the surface. The ES term, on the other hand, is independent of  $\Theta$  but depends on  $\Phi$ . The CV term was derived from the phenomenological arguments in Ref. 5 or Ref. 24. It decreases with  $\Theta$  and may even change sign. The local stability properties of the flat surface can be inferred from the equation for the Fourier modes  $h(q_x, q_y)$  of the height profile, co-moving with the average surface erosion,

$$\partial_t h(q_x, q_y) = -\Gamma(q_x, q_y)h(q_x, q_y), \quad (1)$$

with the quadratic form

$$\Gamma(q_x, q_y) = q_x^2(v_x(\Theta) + A_x(\Theta) - S_{xx}) + q_y^2(v_y(\Theta) + A_y(\Theta) - S_{yy}) + 2q_x q_y S_{xy}. \quad (2)$$

Here,  $v_x, v_y$  are erosion terms;  $A_x, A_y$  denote CV terms; and each  $S$  describes an ES diffusion term, all in lowest non-trivial order of gradient expansions. For more details, in particular on the  $\Theta$  dependence of terms, see Refs. 3, 5, 24, and 25. It should be remarked here, that some patterns displayed in Fig. 3 show rather large slopes and thus may reach the limit of applicability of the continuum model. Note that  $\Gamma > 0$  means smoothing or stability, whereas  $\Gamma < 0$  leads to pattern formation. We now argue that this model is not flexible enough to explain all our observed pattern formation scenarios. The reason for the insufficient flexibility is because the erosion terms and the CV smoothing term have been constructed for amorphous solids and thus only depend on the incidence angle and not on crystal orientation. On the other hand, the ES barriers only depend on crystal orientation and not on  $\Theta$ . This leads to eigenvalues of the quadratic form  $\Gamma$  for arbitrary ES

coefficients with  $\Theta$  dependencies, which are simply and rather universally related. In particular, if  $S_{xy} = 0$ , the ES terms will only cause  $\Theta$  independent shifts of the eigenvalues, whereas all eigenvalues for nonvanishing  $S_{xy}$  are related by an additional  $\Theta$ -independent rescaling.

Plots of the eigenvalues of the quadratic form  $\Gamma$  vs.  $\Theta$  are given in Fig. 7, with and without ES diffusion. Here, we used the erosion terms as calculated in Ref. 25 and the  $\Theta$  dependence of the CV term as obtained in Ref. 24. Without ES barriers, when the pattern formation is determined by curvature-dependent sputter yield and CV smoothing, a stable region with smooth surfaces occurs for small and large ion incidence angles. In the intermediate region (here, between  $30^\circ$  and  $55^\circ$ ) pattern formation is found because of the negative eigenvalue of  $\Gamma$ . The ES barriers of a crystal surface can be introduced by an appropriate choice of  $S$  values. One may now start from any of the observed pattern formation scenarios. For example, many of the surfaces [e.g., Cu(100)] stayed flat for all  $\Theta$  we have tested. This might already contradict the prediction of the model, which shows pattern formation at intermediate angles. However, instability may occur in a  $\Theta$  region between  $45^\circ$  and  $62^\circ$ , so we may have missed it. But from whichever of the observed scenarios we start, it is impossible to generate all the other observed sequences of instabilities (e.g., from flat to ripples as well as from ripples to flat with increasing  $\Theta$ ) by rigidly shifting the graphs of the eigenvalues upward or downward (the rescaling cannot change the  $\Theta$  values at which instabilities occur). Thus, we conclude that the models of Rusponi and Valbusa<sup>18,20</sup> have to be extended and that physical mechanisms beyond ES diffusion, which are sensitive to surface orientation as well as incidence angle (like, e.g., crater functions<sup>24</sup>), have to be added.

Because the sputtered Cu surfaces contain up to 20 at% Ga, we need to consider whether the pattern formation is influenced by this impurity. The absence of additional diffraction peaks for the two investigated TEM samples is consistent with the idea that no Ga phases have formed but does not rule out possible contributions from Ga in solution.<sup>9</sup> Until now, co-deposition of metal impurities has been investigated mainly on Si surfaces and shows that pattern formation can be enhanced, reduced, or completely changed depending on the co-sputtered species and concentration.<sup>9,11</sup> Whether this applies in our studies will be discussed here. First, we observed the same patterns for Cu(110) as Rusponi and co-workers<sup>20</sup> for much lower Ar impurity concentrations, suggesting that Ga is not decisive in determining patterns, at least for this orientation. Second, Ga is distributed homogeneously in the surface and does not correlate with the surface patterns, as has been observed in binary systems in which composition and pattern structure are strongly coupled.<sup>26</sup> However, we cannot exclude the possibility that the average Ga concentration influences the pattern-type formation. This issue could be investigated further by measurements using Ar ions in the same energy range. For the present work, we can state that we observed very significant orientation dependences at (nearly) fixed average Ga concentrations, which thus cannot be caused by Ga impurities.

## V. CONCLUSION

In this paper, we have shown that ion erosion of single-crystal Cu surfaces strongly depends on crystal orientation. At normal ion incidence, surfaces either develop well-pronounced patterns or become smooth. Similar patterns are found at surfaces with crystal orientations close to each other. Ion beam tilting induces multiple pattern changes, which are specific to the crystal orientation. In the case of Cu(100), the surface stays flat for all incidence angles. This non-roughening behavior, as well as the complexity of the pattern changes of other surface orientations, cannot be explained by common continuum models. This indicates the necessity of including patterning mechanisms in addition to ES barriers that depend on surface orientation. The lack of correlation between Ga distribution and pattern features indicates that near-surface Ga enrichment produced during FIB sputtering does not determine the orientation dependence of the patterns.

## ACKNOWLEDGMENTS

We thank Volker Radisch for FIB fabrication of the TEM lamella, Matthias Hahn for STEM and EDX measurements, Burkhard Roos for TEM images, and Reiner Mönig (Karlsruhe Institute of Technology) for the early EBSD studies.

\*reiner.kree@theorie.physik.uni-goettingen.de

<sup>1</sup>W. L. Chan and E. Chason, *J. Appl. Phys.* **101**, 121301 (2007).

<sup>2</sup>H. Fouckhardt, I. Steingoetter, M. Brinkmann, M. Hagemann, H. Zarschizky, and L. Zschiedrich, *Adv. OptoElectron.* **2007**, 27316 (2007).

<sup>3</sup>R. M. Bradley and J. M. E. Harper, *J. Vac. Sci. Technol. A* **6**, 2390 (1988).

<sup>4</sup>P. Sigmund, *J. Mater. Sci.* **8**, 1545 (1973).

<sup>5</sup>G. Carter and V. Vishnyakov, *Phys. Rev. B* **54**, 17647 (1996).

<sup>6</sup>M. Moseler, P. Gumbsch, C. Casiraghi, A. C. Ferrari, and J. Robertson, *Science* **309**, 1545 (2005).

<sup>7</sup>F. Frost, B. Ziberi, A. Schindler, and B. Rauschenbach, *Appl. Phys. A* **91**, 551 (2008).

<sup>8</sup>B. Ziberi, M. Cornejo, F. Frost, and B. Rauschenbach, *J. Phys.: Condens. Matter* **21**, 224003 (2009).

<sup>9</sup>S. Macko, F. Frost, B. Ziberi, D. F. Förster, and T. Michely, *Nanotechnol.* **21**, 085301 (2010).

<sup>10</sup>B. Ziberi, F. Frost, Th. Höche, and B. Rauschenbach, *Phys. Rev. B* **72**, 235310 (2005).

<sup>11</sup>H. Hofsäss and K. Zhang, *Appl. Phys. A* **92**, 517 (2008).

<sup>12</sup>C. S. Madi, E. Anzenberg, K. F. Ludwig Jr., and M. J. Aziz, *Phys. Rev. Lett.* **106**, 066101 (2011).

<sup>13</sup>R. L. Schwoebel and E. J. Shipsey, *J. Appl. Phys.* **37**, 3682 (1966).

<sup>14</sup>T. Michely and J. Krug, *Islands, Mounds, and Atoms: Patterns and Processes in Crystal Growth Far from Equilibrium*, (Springer-Verlag, Berlin, 2004).

<sup>15</sup>O. Malis, J. D. Brock, R. L. Headrick, M. S. Yi, and J. M. Pomeroy, *Phys. Rev. B* **66**, 035408 (2002).

<sup>16</sup>M. Strobel, K.-H. Heinig, and T. Michely, *Surf. Sci.* **486**, 136 (2001).

<sup>17</sup>J. Villain, *J. Phys. I* **1**, 19 (1991).

<sup>18</sup>U. Valbusa, C. Boragno, and F. Buatier de Mongeot, *J. Phys.: Condens. Matter* **14**, 8153 (2002).

<sup>19</sup>H. J. Ernst, F. Fabre, and J. Lapujoulade, *Surf. Sci. Lett.* **275**, L682 (1992).

<sup>20</sup>S. Rusponi, G. Costantini, C. Boragno, and U. Valbusa, *Phys. Rev. Lett.* **81**, 2735 (1998).

<sup>21</sup>V. G. M. Sivel, J. van den Brand, W. R. Wang, H. Mohdadi, F. D. Tichelaar, P. F. A. Alkemade, and H. W. Zandbergen, *J. Microsc.* **214**, 237 (2004).

<sup>22</sup>C. A. Volkert and A. M. Minor, *MRS Bulletin* **32**, 389 (2007).

<sup>23</sup>T. B. Massalsky, H. Okamoto, P. R. Subramanian, and L. Kacprzak, *Binary Alloy Phase Diagrams*, (ASM International, Metals Park, OH, 1990).

<sup>24</sup>B. Davidovitch, M. J. Aziz, and M. P. Brenner, *Phys. Rev. B* **76**, 205420 (2007).

<sup>25</sup>M. A. Makeev, R. Cuerno, and A. L. Barabasi, *Nucl. Instrum. Methods Phys. Res., Sect. B* **197**, 185 (2002).

<sup>26</sup>Q. Wie, J. Lian, W. Lu, and L. Wang, *Phys. Rev. Lett.* **100**, 076103 (2008).

<sup>27</sup>P. Stolze, *J. Phys. Condens. Matter* **6**, 9495 (1994).